Materials Advances

PAPER

View Article Online
View Journal | View Issue

Check for updates

Cite this: *Mater. Adv.*, 2020, 1, 421

Received 29th March 2020,
Accepted 29th April 2020

DOI: 10.1039/d0ma00140f

rsc.li/materials-advances

Nanoscopically and uniformly distributed SnO_2@TiO_2/C composite with highly mesoporous structure and bichemical bonds for enhanced lithium ion storage performances†

Meisheng Han,[ab] Yongbiao Mu[a] and Jie Yu *[ac]

The ultralow volume deformation (<4%) and low cost have aroused great interest in using TiO_2 as the anode of lithium ion batteries (LIBs), but its low capacity (168 mA h g^{-1}), no more than half of the theoretical capacity, limits its practical application in high-energy-density LIBs. In order to solve this problem, here we propose a one-step method for fabrication of the SnO_2@TiO_2/C nanocomposite, which features a superior nanoarchitecture with mesopores, interfacial chemical bonds, vast phase boundaries, carbon coating, and ultrasmall nanocrystals. These nanostructures endow SnO_2@TiO_2/C with a high capacity of 830.7 mA h g^{-1} at 0.5C after 100 cycles, excellent cyclability over 1000 cycles with negligible capacity loss per cycle (0.004%) at 10C, and a high lithium ion transport rate within a few seconds for one cycle. Importantly, the full cell with prelithiated SnO_2@TiO_2/C as the anode and commercial $LiCoO_2$ as the cathode achieves a high energy density of 328.4 W h kg^{-1} at 0.1C and 245.9 W h kg^{-1} at 1C, which are superior to those of previously reported TiO_2-based materials.

Introduction

Titanium dioxide (TiO_2) has been regarded as a promising anode material in rechargeable lithium ion batteries (LIBs) due to its low cost, non-toxicity, and ultralow volume change (<4%) during lithium ion intercalation/deintercalation.[1,2] TiO_2 possesses a series of allotropes, such as anatase,[3,4] rutile,[5,6] and TiO_2-B.[7,8] Among them, anatase TiO_2 has been widely investigated due to its inherent crystal structure for lithium ion storage.[9,10] However, the low theoretical capacity (168 mA h g^{-1}) corresponding to the formula of $Li_{0.5}TiO_2$ of anatase TiO_2 cannot meet the ever-increasing demand of high-energy-density LIBs, thus limiting its practical use.[3] In order to enhance the capacity of TiO_2, a large number of efforts have been made: (i) preparing nanostructures like nanoparticles,[3] nanotubes,[4] nanosheets,[11] and nanomembranes;[12] (ii) fabricating mesoporous composites;[13,14] (iii) forming phase boundaries;[11] and (iv) constructing interfacial chemical bonds.[1,15] Specifically, the design of nanostructures and mesoporous structure is intended to increase the contact area of active material with the electrolyte and shorten the transport distance of lithium ions, thus ensuring sufficient reaction between lithium ions and the active material to increase the reversible capacity. Additionally, the capacity can be enhanced by diminishing the particle size to the nanoscale, which can increase the number of interfaces between materials to accommodate more lithium ions.[16,17] Similarly, introducing multi-phase compounds can increase the capacity by generating numerous phase boundaries to provide additional lithium ion storage sites.[11] Furthermore, the formation of chemical bonds between multiple phases can create a strong interfacial force, which can not only enhance the structural stability of the active material and achieve high capacity retention, but also can enhance the capacity by increasing the diffusion depth of lithium and enabling more active materials to react with lithium ions.[1,15] Accordingly, a TiO_2-based anode with these structures can be assumed to deliver satisfactory capacity. Thus far, several TiO_2-based anode materials with similar structures have been reported. For example, anatase TiO_2 nanoparticles with mesoporous structure prepared by atomic layer deposition based on a sacrificial carbon template were shown to have a capacity of 158.4 mA h g^{-1} with a capacity retention of 80% after 100 cycles at 1C and a rate capability of 105 mA h g^{-1} at 5C.[3] Additionally, a nanocomposite with ultrathin anatase TiO_2 nanosheets embedded into TiO_2-B nanodomains and vast phase boundaries formed within them was also reported to enhance the lithium ion storage capacity, with a specific capacity of 280 mA h g^{-1} at 0.5C and 190 mA h g^{-1} after 1000 cycles and a

---

[a] *Songshan Lake Materials Laboratory Dongguan, Guangdong 523808, China*
[b] *Beijing National Laboratory for Condensed Matter Physics, Institute of Physics, Chinese Academy of Sciences, Beijing 100190, China*
[c] *Shenzhen Engineering Lab for Supercapacitor Materials, Shenzhen Key Laboratory for Advanced Materials, School of Material Science and Engineering, Harbin Institute of Technology, Shenzhen, University Town, Shenzhen 518055, China. E-mail: jyu@hit.edu.cn*

† Electronic supplementary information (ESI) available. See DOI: 10.1039/d0ma00140f

capacity retention of 86% at 10C.[11] Moreover, a TiO_2/graphene nanocomposite with strong Ti–O–C chemical bonds in the interfaces synthesized by a hydrothermal reaction exhibited a capacity of 206.7 mA h g^{-1} at 3C and 140.3 mA h g^{-1} after 100 cycles and a capacity retention of 87.7% at 30C.[18] Furthermore, a high capacity of 227.2–274.0 mA h g^{-1} with good cyclability and rate performance during 200–800 cycles at a current density of 10C or lower was obtained by a TiO_2@C nanocomposite prepared by a hydrothermal reaction followed by carbonization[13] and a TiO_2@reduced graphene oxide nanocomposite synthesized by aerosol-assisted spray drying followed by calcination.[19]

Despite the improved lithium ion storage capacity, the above-mentioned TiO_2-based nanocomposites are still low in capacity at various current densities. Besides, the synthesis steps of these nanocomposites were complex, involving sonicating, stirring, centrifuging, washing, drying, calcinating, and etching, coupled with some repeated operations, suggesting the necessity of a simple fabrication route for preparing high-capacity TiO_2-based nanocomposites with the above-mentioned structures (i–iv) to promote their practical application.

Herein, we propose a one-step method for fabricating a highly mesoporous SnO_2@TiO_2/C nanocomposite with SnO_2 nanocrystals homogeneously dispersed in the TiO_2/C matrix and an average size of about 10 nm. The coexistence of multiple phases in the nanocomposites induces numerous phase boundaries and thus the formation of Sn–O–C and Ti–O–C chemical bonds. The addition of high-capacity SnO_2 (13.0 wt%), coupled with these structural advantages, endows the SnO_2@TiO_2/C nanocomposite with a reversible capacity of 830.7 mA h g^{-1} after 100 cycles at 0.5C, higher than any of the reported TiO_2-based anodes at a similar cycle number and current density. Furthermore, SnO_2@TiO_2/C is also shown to deliver excellent cyclability and rate performance in half and full cells.

Experimental

Materials

Tetrabutyl orthotitanate tetramer ($C_{40}H_{90}O_{13}Ti_4$, 99.9%, TOT) and monobutyltin oxide ($C_4H_{10}O_2Sn$, 99.9%, MO) were purchased from Tokyo Chemical Industry (Tokyo, Japan); the electrolyte (1 M $LiPF_6$ in a mixture of ethylene carbonate/diethylene carbonate/dimethyl carbonate at a volume ratio of 1 : 1 : 1) from DoDoChem; acetylene black, Li foil, Cu foil, Al foil, polyvinylidene fluoride (PVDF), the Celgard 2400 membrane, *n*-methyl-2-pyrrolidone (NMP), and lithium cobaltate ($LiCoO_2$) from MTI Corporation; and the stabilized lithium metal power (SLMP) from FMC Lithium Co.

Preparation of TiO_2/C and SnO_2@TiO_2/C

The precursor solution was obtained by dissolving 0.2 g MO in 1 g TOT, then transferring the solution into a reaction vessel and sealing it in a glove box under an argon environment. SnO_2@TiO_2/C was prepared by heating the vessel to 600 °C at 10 °C min^{-1}, maintaining it for 0.5 h in a tube furnace with flowing Ar, and then cooling to room temperature naturally. Meanwhile, TiO_2/C was synthesized by heating pure 1 g TOT under the same conditions.

Characterization

The morphology, structure, and composition of the obtained samples were characterized using a scanning electron microscope (SEM, Hitachi S-4700), transmission electron microscope (TEM, FEI Talos F200x) with an X-ray energy dispersive spectrometer (EDS), accelerated surface area and porosimetry system (Micromeritics ASAP 2010), X-ray diffractometer (XRD, D/max-2500/PC, Rigaku), Raman spectrometer (Renishaw RM-1000), X-ray photoelectron spectrometer (XPS, Thermo Scientific Escalab 250Xi), thermogravimetric analyzer (TGA, STA449 F3 Jupiter), and inductively coupled plasma atomic emission spectrometer (ICP-AES). The electrical conductivity of the samples was tested with a powder electrical resistivity tester (ST-2722, Suzhou Jingge Electronic Co., Ltd, China).

Electrochemical measurements

The electrodes were prepared by coating a mixture of active materials, acetylene black, and PVDF at a weight ratio of 8 : 1 : 1 on Cu foil, followed by drying at 80 °C for 12 h in a vacuum oven. The mass of active material loaded on each electrode was about 1.2 mg cm^{-2}. The electrochemical performances were measured *via* assembling a 2032 coin-type cell in a glove box filled with pure argon, which consisted of the prepared electrode, Li foil, a Celgard 2400 membrane, and the electrolyte. The electrochemical performances of the cells were measured on a Land CT2001A battery-test system (Wuhan Land Electronic Co., China) in the voltage range of 0.01–3.00 V (*vs.* Li/Li^+) and at current densities of 1–50C (1C = 168 mA g^{-1}). The electrochemical impedance spectra (EIS) were measured in the frequency range of 10^5 to 10^{-2} Hz with an amplitude of 5 mV, and the cyclic voltammogram (CV) in the voltage range of 0.01 to 3.00 V (*vs.* Li/Li^+) at scanning rates of 0.1–10 mV s^{-1} on a CHI 760D electrochemical workstation (Shanghai CH Instruments Co., China). In the full cell, the cathode electrode consisted of $LiCoO_2$ (90 wt%), PVDF (5 wt%), and acetylene black (5 wt%) on Al foil, and the N/P ratio was 1.1 at a mass loading of 2.0 and 10.5 mg cm^{-2} for SnO_2@TiO_2/C and $LiCoO_2$, respectively. Before assembling the coin-type full cell, the SnO_2@TiO_2/C electrode was pre-lithiated by using the commercial SLMP to improve its first coulombic efficiency (CE). The specific process has been reported in our previous report.[15] For full-cell testing, the cycling curves were measured at 0.1C (1C = 0.14 A g^{-1}) and rate curves were tested at 0.2–1C in the voltage window of 1.0–3.6 V. All cells were tested at room temperature.

Results and discussion

Fig. 1 shows the SEM images of TiO_2/C. In Fig. 1a, TiO_2/C exhibits a spherical shape with an average size of 2.5 μm due to the high vapor pressure, with its formation mechanism being discussed in detail in our previous reports.[20,21] Interestingly, adding MO into TOT led to the formation of nanoparticles with

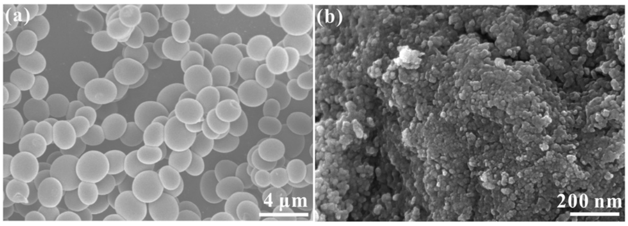

Fig. 1 SEM images of TiO_2/C (a) and $SnO_2@TiO_2/C$ (b).

an average size of 15 nm (Fig. 1b), indicating that MO addition facilitates nanocomposite formation in the vapor pressure-induced reaction process.[15]

In the XRD patterns (Fig. 2a), the two samples show diffraction peaks at 25.3, 37.8, 48.1, 53.9, 54.9, 62.6, 68.7, 75.1, and 82.7°, corresponding, respectively, to the (101), (004), (200), (105), (211), (204), (116), (215), and (224) crystal planes of anatase TiO_2 (JCPDS: 21-1272), suggesting the successful synthesis of anatase TiO_2. Besides, $SnO_2@TiO_2/C$ exhibits four peaks at 26.6, 33.8, 51.8, and 66.1°, corresponding, respectively, to the (110), (101), (211), and (301) crystal planes of crystalline SnO_2 (JCPDS No. 41-1445), indicating the formation of SnO_2. In the Raman spectra with the insert for the enlarged image of $SnO_2@TiO_2/C$ in the range of 100–835 cm^{-1} (Fig. 2b), the two samples show obvious Raman peaks of anatase TiO_2 at around 148.7, 392.4, 506.6, and 630.9 cm^{-1} (Fig. 2b), corresponding to the E_g, B_{1g}, A_{1g}, and E_g modes,[3,12] as well as two peaks around 1323.8 and 1590.5 cm^{-1}, corresponding to the D and G peaks of carbon materials,[15,22,23] respectively, indicating the existence of anatase TiO_2 and free carbon. Obviously, $SnO_2@TiO_2/C$ exhibits the Raman peak of SnO_2 at about 770 cm^{-1}, suggesting the presence of SnO_2 in the sample. Meanwhile, the D peak arises from a double resonance process involving a phonon and a defect, while the G peak is attributed to in-plane vibrations and E_{2g} symmetry. Due to the overlap of the D and G peaks, peak fitting was performed, and additional peaks appeared at about 1240 and 1500 cm^{-1}, labeled as I and D″, respectively. The I peak is related to disorder in the graphitic lattice or sp^2–sp^3 bonds,[22,23] while the D″ peak is known to occur in the presence of amorphous carbon.[22,23] Besides, the intensity ratios of the D and G (I_D/I_G) peaks indicate the disorder degree of the graphitic structure,[22,23] which are close to each other for the two samples (0.68 for $SnO_2@TiO_2/C$ and 0.67 for TiO_2/C), suggesting a similar disorder degree for the carbon in both of them. Furthermore, the high ratio of I_D/I_G indicates the existence of vast defects in the carbon, which favors lithium ion storage.

The contents of the elements in the precursor and the two samples are shown in Table S1, ESI.† The obtained samples are seen to retain the elements of the precursor apart from H. Furthermore, compared with the precursor, the obtained samples show an increase in the mass percentages of Ti and Sn elements while a decrease in the mass percentages of C and H. These results suggest that a large number of C,H-containing substances were produced by the decomposition of the precursors at a high temperature, which could not be converted into solids under high pressure, leading to a decrease in the mass of C and H.

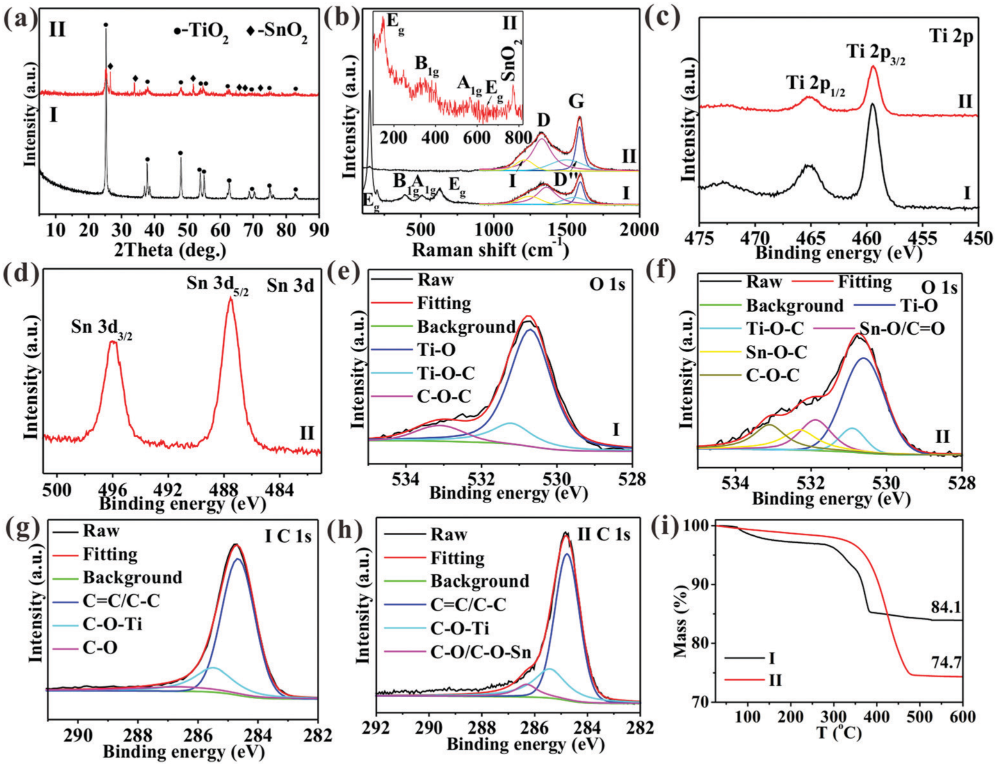

Fig. 2 (a) XRD, (b) Raman spectra, (c–h) XPS spectra of Ti 2p (c), Sn 3d (d), O 1s (e and f), and C 1s (g and h), and (i) TG curves of TiO_2/C (I) and $SnO_2@TiO_2/C$ (II).

According to the XPS results (Fig. S1, ESI†), the atomic ratio of O and Ti is around 2.11, approaching the theoretical value of TiO_2, and the atomic ratio of O and Sn is about 2.02, close to the theoretical value of SnO_2, indicating the formation of TiO_2 and SnO_2. Additionally, the two samples show two XPS peaks around 465.2 and 459.4 eV due to the binding energies of Ti $2p_{3/2}$ and Ti $2p_{1/2}$ of anatase TiO_2,[1,3] respectively (Fig. 2c), further suggesting the formation of anatase TiO_2. The SnO_2@TiO_2/C samples exhibit two Sn 3d peaks of Sn^{4+} $3d_{3/2}/3d_{5/2}$ at around 495.9/487.5 eV (Fig. 2d), again indicating the formation of SnO_2.[24,25] The two samples also show a wide peak of O 1s from 528.8 to 534.4 eV, which can be fitted using five peaks (Fig. 2e and f): Ti–O bonds at 530.7 eV,[26,27] Ti–O–C bonds at 531.2 eV,[26,27] Sn–O/C=O at 531.5 eV,[28] Sn–O–C at 532.3 eV,[28] and C–O–C at 533.1 eV,[26,28] confirming the formation of Ti–O–C and Sn–O–C bonds. The C 1s peaks of the two samples are fitted using three peaks (Fig. 2g and h): C=C/C–C at 284.8 eV,[22] Ti–O–C at 285.4 eV,[26,29] and C–O/C–O–Sn at 286.2 eV,[30] further confirming the formation of the Ti–O–C and Sn–O–C bonds. The percentage of Ti–O–C bonds increases from 20.7 for TiO_2/C to 25.5% for SnO_2@TiO_2/C (Table S2, ESI†), due to the production of more interfaces between TiO_2 and C by the smaller-sized TiO_2 nanoparticles in SnO_2@TiO_2/C. Additionally, the Sn–O–C bonds increase from 0 to 4.1% with the addition of MO into TOT (Table S2, ESI†). The high content of Ti–O–C and Sn–O–C bonds favors lithium ion storage. Since the XPS technique can only detect the surface (several nanometers) composition of the material, the XPS spectra of SnO_2@TiO_2/C in the deeper area were also tested to further confirm the presence of chemical bonds of Ti–O–C and Sn–O–C bonds inside the sample. Briefly, the sample powders were compressed into a thin plate, followed by bombarding it with argon ions for 30 min, and testing the bombarded area by XPS. The XPS results (Fig. S2, ESI†) are consistent with the data in Fig. 2c–h, indicating that the chemical bonds of Ti–O–C and Sn–O–C are distributed in the whole SnO_2@TiO_2/C sample. ICP-AES results reveal the mass percentages of Sn/Ti as 0/50.3 and 10.2/36.8 wt%, indicating that the mass contents of SnO_2/TiO_2/C are 0/83.9/16.1 wt% and 13.0/61.3/25.7 wt%, corresponding to TiO_2/C and SnO_2@TiO_2/C, respectively (Table S3, ESI†). The TG curves (Fig. 2i) show that the mass percentages of the residuals post high temperature oxidation are 84.1 and 74.7%, corresponding to TiO_2/C and SnO_2@TiO_2/C, respectively, suggesting that the respective carbon content is 15.9 and 25.3 wt%, which are consistent with the ICP-AES results.

Fig. 3 shows the high angle annular dark field (HAADF) image and its corresponding EDS mapping images. Ti, O, and C elements are seen to be uniformly distributed on the surface of TiO_2/C spheres (Fig. 3a–d). The average size of TiO_2 particles in the TiO_2/C spheres is shown to be about 45 nm by measuring the crushed powder, with a decrease of 10 nm in the size of the nanoparticles after adding MO into TOT (Fig. 3f), which agrees with the SEM observation (Fig. 1b). In Fig. 3g, carbon layers can be seen at the edge of the sample, confirming the presence of the carbon coating. Fig. 3h shows the lattice fringes of the (101) crystal plane of anatase TiO_2 and (110) crystal plane of SnO_2, corresponding, respectively, to the highest diffraction peaks of TiO_2 at 25.3° and SnO_2 at 26.6° (Fig. 2a). Besides, it can be clearly observed that the nanocrystals are well interconnected by C, combined with the existence of vast chemical bonds of Ti–O–C and Sn–O–C, suggesting that the nanocomposite possesses the superior nanoarchitecture of C/C–O–Ti/TiO_2/Ti–O–C/C/C–O–Sn/SnO_2/Sn–O–C/C. In Fig. 3i, the selected area electron diffraction (SAED) pattern shows the Debye–Scherrer ring patterns of the (101), (004) and (211) crystal planes of anatase TiO_2 as well as the (110) and (221) crystal planes of SnO_2, further confirming the existence of TiO_2 and SnO_2 nanocrystals. In Fig. 3j–n, HAADF and its corresponding EDS elemental mapping images show the even

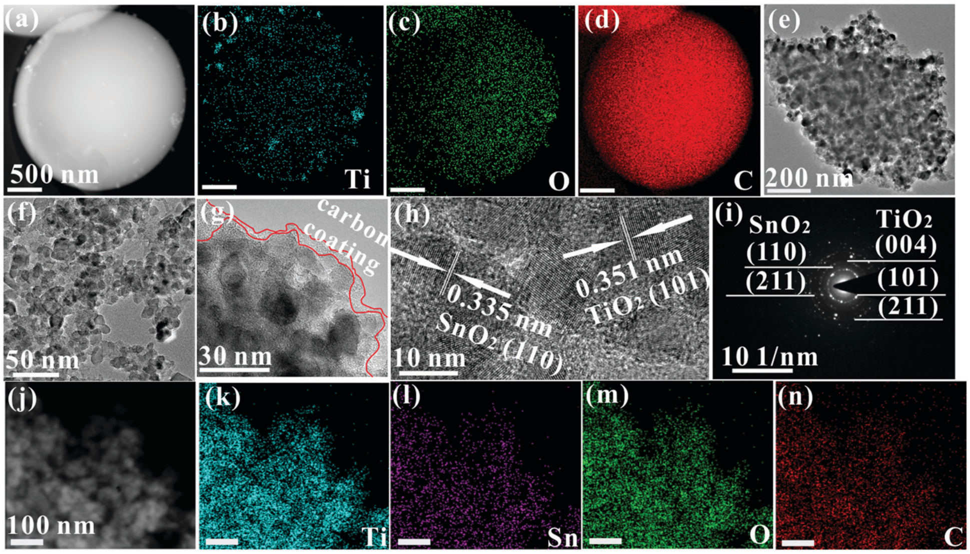

Fig. 3 (a) High angle annular dark field image and the corresponding EDS elemental mapping images of Ti (b), O (c), and C (d) of TiO_2/C spheres; (e) TEM image of crushed TiO_2/C spheres; (f) TEM image, (g and h) HRTEM image, and (i) the corresponding SAED pattern of SnO_2@TiO_2/C; and (j) HAADF image and the corresponding EDS elemental mapping images of Ti (k), Sn (l), O (m), and C (n) of SnO_2@TiO_2/C.

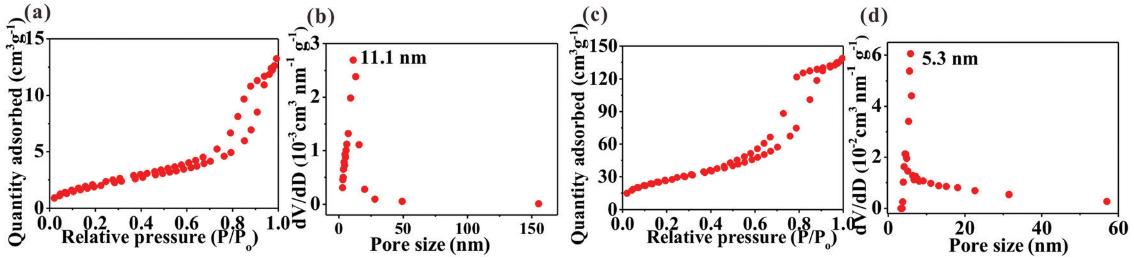

Fig. 4 Nitrogen adsorption–desorption isotherms and pore-size distribution of TiO_2/C (a and b) and SnO_2@TiO_2/C (c and d).

distribution of Ti, Sn, O, and C elements, verifying the homogeneous dispersion of TiO_2, SnO_2, and free carbon in the nanocomposite. The homogeneous dispersion structure at the nanoscale could induce numerous phase boundaries or interfaces, contributing to lithium ion storage.

Fig. 4 shows the Brunauer–Emmett–Teller (BET) surface area and Barrett–Joyner–Halenda (BJH) pore-size distribution of the samples determined by nitrogen adsorption–desorption isotherms. The two samples exhibit a typical type-IV isotherm, indicating that they possess a mesoporous structure. Due to the formation of nanostructure, SnO_2@TiO_2/C has a significantly higher value than TiO_2/C in the BET surface area (143.3 $m^2\ g^{-1}$ *versus* 11.8 $m^2\ g^{-1}$) and pore volume (0.86 $cm^3\ g^{-1}$ *versus* 0.06 $cm^3\ g^{-1}$), with mesopores centered at 5.3 nm for the former and 11.1 nm for the latter. Comparatively, the disadvantage of the highly mesoporous structure of the SnO_2@TiO_2/C nanocomposite involves the increase of the active material specific surface area, contributing to the formation of more solid electrolyte interface (SEI) film during the first cycle and decreasing the first coulombic efficiency (CE). However, this disadvantage can be improved by the commercial prelithiation technique.[15] Accordingly, the low CE of our SnO_2@TiO_2/C anode is not an obstacle to its practical application. More importantly, the porous structure possesses several advantages: (i) favoring the contact of the active material with the electrolyte; (ii) shortening the diffusion distance of Li^+; (iii) facilitating the storage of additional Li^+; and (iv) accommodating the volume change of the active material upon cycling, thus leading to enhanced capacity, cycling life, and rate performance.[13,14] Collectively, the preparation of a porous structure is favorable for lithium ion storage.

Fig. 5 shows the charge/discharge and cycling curves of the two samples. Different from the first charge/discharge curve of TiO_2/C, SnO_2@TiO_2/C exhibits two potential plateaus below 0.6 V in the charge/discharge curves, attributed to the delithiation/lithiation of SnO_2.[21,31] Additionally, SnO_2@TiO_2/C does not show obvious delithiation plateaus of anatase TiO_2 at 2.15 V, probably due to the contribution of SnO_2 and higher carbon content.[15] The reversible capacity of the active material has been reported to be associated with the relative content of each component, the particle size, and the number of phase boundaries and chemical bonds at the interface.[15,21] Due to low theoretical capacity of anatase TiO_2, adding high-capacity active material can greatly enhance the capacity of TiO_2-based anodes, such as SnO_2 and amorphous carbon. Owing to the low electrical conductivity (EC) of anatase TiO_2, adding materials with higher EC can considerably improve the electrical connectivity of the whole electrode, enabling more active materials to react with lithium ions and thus increasing the specific capacity.[21] The EC is shown to increase with a rise in the carbon content (Table S4, ESI†). As previously reported, active materials with a nanoscale size possess higher specific capacity than their corresponding bulk materials, because nano-sized materials can remarkably

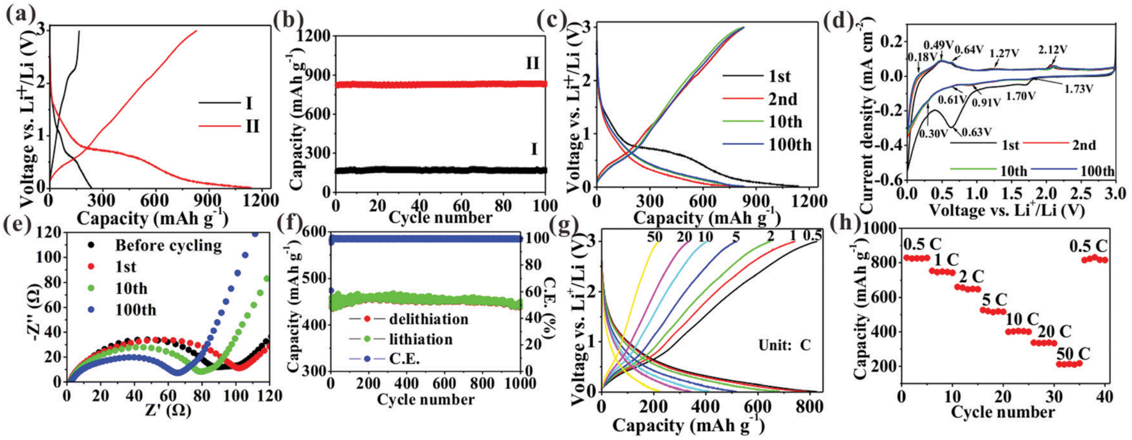

Fig. 5 (a) First charge/discharge curves; (b) cycling curves at 0.5C of TiO_2/C (I) and SnO_2@TiO_2/C (II); (c) charge/discharge curves at different cycles; (d) CV curves; (e) Nyquist plots; (f) cycling performance at 10C; (g) charge/discharge curves at different current densities; and (h) rate performance of SnO_2@TiO_2/C.

shorten the lithium ion diffusion distance and achieve deeper lithiation to enhance the capacity.[3,4] Introducing more components into the active materials can generate more phase boundaries to store extra lithium ions and enhance the reversible capacity.[11] The formation of chemical bonds in the interface of each phase can increase the interfacial defects, EC, and structure stability, thus achieving higher capacity and cyclability.[1,15] In Fig. 5b and Table S5, ESI,† SnO_2@TiO_2/C is seen to have a higher specific capacity (830.7 mA h g^{-1}) than TiO_2/C (169.6 mA h g^{-1}) after 100 cycles due to its larger amount of SnO_2, C, Sn–O–C, and Ti–O–C bonds as well as higher EC (Tables S2–S4, ESI†).

The electrochemical performance of SnO_2@TiO_2/C was further investigated. Fig. 5c shows its voltage profiles at different cycle numbers. The first discharge and charge capacities are 1141.2 and 823.4 mA h g^{-1}, respectively, with a first CE of 72.2%. The low CE has been reported to arise from the formation of an SEI layer and Li_2O.[15,21] The subsequent charge/discharge curves retain a similar shape, indicating the high stability of the electrode structure during cycling. After 100 cycles, a high reversible capacity of 830.7 mA h g^{-1} is observed, corresponding to a capacity retention of 100.9%. The increased post-cycling capacity may result from interfacial Li^+ storage and electrochemical activation.[15] In the present study, the obtained reversible capacity (830.7 mA h g^{-1}) is higher than that of any previously reported TiO_2-based anode (Table S6, ESI†), due to the formation of a large number of phase boundaries, chemical bonds, and mesoporous sites in the nanocomposite, facilitating the storage of more lithium ions and thus increasing the capacity.[1,11,13] Additionally, adding a high amount of SnO_2 and C also contributes to the enhancement of the capacity, leading to a high reversible capacity of 1419.5 mA h g^{-1} for the SnO_2/C nanocomposite (Fig. S3, ESI†). Fig. 5d shows the CV curves of SnO_2@TiO_2/C, with the presence of the characteristic anodic peaks at about 2.12 V and cathodic peaks at about 1.73 V of anatase TiO_2.[9,10] Besides, the three anodic peaks and two cathodic peaks below 0.7 V belong to the delithiation and lithiation behaviors of SnO_2, respectively.[21,31] Interestingly, the presence of a pair of oxidation and reduction peaks at 1.27 and 0.91 V is not the typical delithiation/lithiation behavior of TiO_2, SnO_2, or C, which may be attributed to the formation of a new reversible lithium ion storage site by phase boundaries, defects, interfacial chemical bonds, and the mesoporous structure. Fig. 5e shows the Nyquist plots at different cycle numbers. The EIS were fitted to an equivalent circuit (Fig. S4, ESI†), where R_s is the electrolyte resistance, corresponding to the intersection of the high-frequency oblique line and the horizontal axis;[32] R_{ct}, the charge transfer resistance, corresponding to the diameter of the depressed semicircle;[32] and W, the Warburg impedance of Li^+ ion diffusion, corresponding to the low-frequency slope line.[32] The values of R_s and R_{ct} at different cycle numbers are shown in Table S7, ESI.† With a rise in the cycle number, the R_s value is shown to gradually increase, suggesting the increase of the electrolyte resistance with increasing cycling number. Meanwhile, the R_{ct} value is seen to increase after the 1st cycle due to the formation of an SEI layer, followed by a gradual decrease, probably due to electrochemical activation on cycling.[15] The decrease of R_{ct} favors the enhancement of the capacity and cyclability. In Fig. 5f, a long cycling life is shown at 10C, with a high specific capacity of 438.5 mA h g^{-1} at a 0.004% capacity loss per cycle after 1000 cycles as well as an average CE of 99.72% during 2–1000 cycles, indicating the high reversibility of the electrode during cycling. The lithium ion transport of SnO_2@TiO_2/C was investigated by measuring the rate capability at current densities of 0.5 to 50C (Fig. 5g and h), and the shape of the charge/discharge curves remains unchanged at different current densities, indicating that the electrode structure is stable during rate testing. The rate capacities are measured as 827.4, 742.2, 647.8, 516.8, 400.6, 333.5, and 217.7 mA h g^{-1} at 0.5, 1, 2, 5, 10, 20, and 50C, respectively, with a high capacity of 217.7 mA h g^{-1} at 50C, sufficiently proving the excellent rate performance of SnO_2@TiO_2/C. Importantly, the specific capacity returns to almost 100% of the initial capacity with the current density back to 0.5C, confirming that the electrode structure is still highly stable even after high current charging and discharging. Our SnO_2@TiO_2/C nanocomposite is superior to other TiO_2-based anodes in cycling and rate performances (Table S6, ESI†). Especially, the rate capability is comparable and even superior to that of other anodes, such as a Sn-based anode, a SiO_x/SiO_y membrane, a Si nanotube, $Nb_{18}W_{16}O_{93}$, a $Li_4Ti_5O_{12}$ nanowire, and a graphite/Si/carbon composite (Table S8, ESI†).

The reasons for the high capacity of SnO_2@TiO_2/C are further explored by estimating the pseudocapacity contribution in the total capacity using CV curves at different scanning rates (Fig. 6a). The relationship between the scanning rate (ν) and peak current (i_p) satisfies the following eqn (1):

$$\log(i) = a\log(\nu) + \log(b) \qquad (1)$$

where a and b are empirical parameters. The 0.5 a-value indicates a diffusion-controlled behavior and the 1 a-value represents an ideal pseudocapacitive behavior. The a-value can be calculated

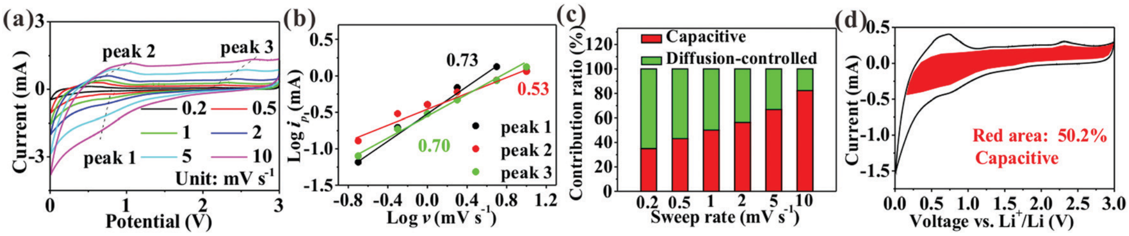

Fig. 6 (a) CV curves at different scanning rates; (b) the line relationship of log(i) *vs.* log(ν) at peaks 1–3 marked in (a); (c) the percentages of the pseudocapacitive contribution at different scanning rates; and (d) the detailed pseudocapacitive contribution at a scanning rate of 1 mV s^{-1} of SnO_2@TiO_2/C.

as the slope from the plots of log(i) *versus* log(v) at peaks 1–3 (Fig. 6b). The a-value for peak 1, peak 2, and peak 3 is calculated as 0.51, 0.53, and 0.70, respectively (Fig. 6b), indicating that the diffusion-controlled and pseudocapacitive behaviors are responsible for the high capacity of SnO_2@TiO_2/C. The relationship of the total capacity at a given v and voltage (V) is shown in the following eqn (2):

$$i\ (\mathrm{V}) = k_1 v^{1/2} + k_2 v \tag{2}$$

where the values of $k_1v^{1/2}$ and k_2v represent the diffusion-controlled and pseudocapacitive process, respectively. An increase of v from 0.2 to 10 mV s^{-1} witnesses an increase from 35.1 to 82.3% in the percentage of the pseudocapacitive contribution (Fig. 6c), suggesting the significant role of pseudocapacitive behavior in the total capacity, especially at a high v. The specific pseudocapacitive contribution at a scanning rate of 1 mV s^{-1} is presented in the red area (Fig. 6d). The high pseudocapacitive contribution in the SnO_2@TiO_2/C nanocomposite can be attributed to the following three reasons: (i) vast phase boundaries between TiO_2, SnO_2, and C can offer extra Li^+ storage sites; (ii) the formation of a large number of interfacial chemical bonds can induce numerous defects as additional Li^+ storage sites; and (iii) the mesoporous structure can accommodate excess Li^+.

The practicality of the SnO_2@TiO_2/C anode was confirmed by testing the delivery capacity of a full cell assembled with a prelithiated SnO_2@TiO_2/C anode and $LiCoO_2$ cathode. The full cell exhibits a high capacity of 142.2 mA h g^{-1}, a capacity retention of 93.3% after 100 cycles at 0.1C (Fig. 7a and b) and a superior rate performance with a capacity of 110.7 mA h g^{-1} at 1C (Fig. 7c and d), which are higher than the values of the reported full cells of graphite/$LiCoO_2$ and graphite/$LiFePO_4$.[33–35] The gravimetric energy density of the full cell can be calculated by the following eqn (3):[36]

$$\text{Energy density }(\mathrm{W\ h\ kg^{-1}})\left(\frac{C_{\text{cathode}} \times m_{\text{cathode}}}{(m_{\text{cathode}} + m_{\text{anode}})}\right) \times V \tag{3}$$

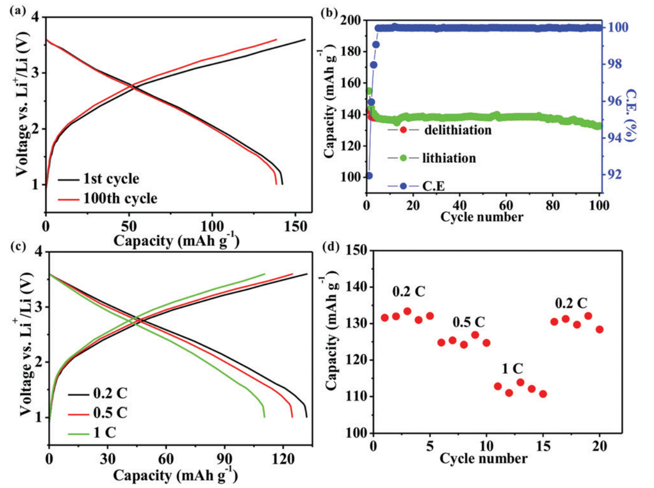

Fig. 7 (a) The charge/discharge curves at 0.1C; (b) the cycling performance at 0.1C; (c) the charge/discharge curves at different current densities; and (d) the rate performance of full cells. The capacity is calculated based on the mass of $LiCoO_2$.

where C_{cathode} is the specific capacity calculated based on the mass of the cathode; V, the nominal voltage of 2.75 V; and $m_{\text{cathode}}/m_{\text{anode}}$, the active mass of the cathode and anode, respectively. Accordingly, the gravimetric energy density is calculated as about 328.4 W h kg^{-1} at 0.1C and 245.9 W h kg^{-1} at 1C, which is comparable to that of a graphite/$LiCoO_2$ full cell (335 W h kg^{-1} at 0.1C),[37–39] and superior to that of the reported full cell of a TiO_2-based anode.[40,41] In previous reports,[41] the nominal voltage is shown as about 2 V in the TiO_2/$LiCoO_2$ full cell. In our case, the enhanced nominal voltage may be ascribed to (i) the addition of low-working potential crystalline SnO_2 (0.2–0.8 V)[21] and amorphous carbon (below 0.5 V) and (ii) the formation of a new lithium ion storage site, with a pair of oxidation and reduction peaks present, respectively, at 1.27 and 0.91 V, as confirmed by the CV curves. It should be mentioned that the energy density should be calculated based on the mass of the whole cell, including both the active materials (cathode material, Li anode and electrolyte) and the inactive materials (conductive carbon, binder, current collectors, tabs, separator and packaging material). However, our research focuses on improving the capacity of anode materials. For the whole battery, when the areal capacity of the active material is constant, the mass of the anode material tends to decrease with an increase of its capacity, which can improve the energy density of the battery. The mass values of the inactive materials and electrolyte should be a fixed value in batteries, but they are absent in eqn (3), because they are unclear for us. In academic studies, researchers are more inclined to use the simplified eqn (3) to calculate the energy density,[33–36] because it still makes sense in that the higher the energy density calculated by this simplified equation, the higher the energy density when calculated with all materials included, suggesting the reference value of this calculated density.

The high stability of the electrode structure was verified by SEM and TEM analysis of the electrode after 2000 cycles at 10C. In the SEM images, the electrode surface is observed to be intact (Fig. S5a and b, ESI†), without any cracks in the nanoparticles (Fig. S5c and d, ESI†). These results confirm the high structural stability of SnO_2/TiO_2/C nanocomposites during cycling, which is ascribed to the unique nanoarchitecture of SnO_2@TiO_2/C (Fig. 8). Specifically, the carbon coating on the surface of TiO_2 and SnO_2 nanocrystals can greatly suppress the structural volume change, enhance the electrical conductivity, and inhibit the aggregation of nanocrystals, thus improving the

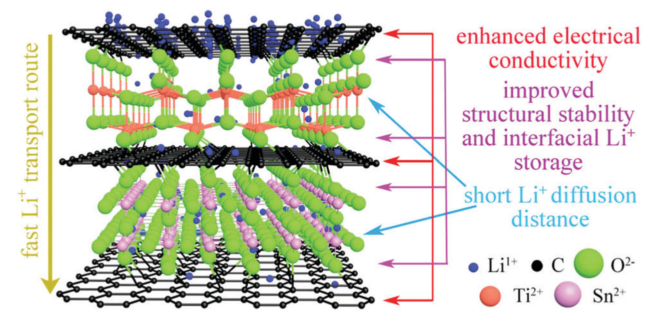

Fig. 8 A schematic illustration of the lithium ion storage mechanism in the SnO_2@TiO_2/C nanoarchitecture.

cyclability and rate performance.[42,43] Additionally, the formation of Ti–O–C and Sn–O–C bonds in the interfaces can promote interfacial charge transfer and enhance the structural stability of SnO_2@TiO_2/C, thus contributing to fast lithium ion transport and long cycling life.[15] Furthermore, the phase boundaries and mesoporous structure can afford the storage of additional Li^+ and thus achieve a high capacity.[42,43] Finally, the ultrasmall nanocrystals can supply enormous active storage sites and shorten the Li^+ diffusion distance, thus facilitating high capacity and enhancing the rate capability.[42,43]

Conclusion

In this research, we propose a one-step pressure-induced vapor phase method for fabricating a chemically bonded SnO_2@TiO_2/C nanocomposite with a highly mesoporous structure as well as SnO_2 and TiO_2 nanocrystals of a size of about 10 nm. The fine multi-component nanocrystals are shown to induce a large amount of phase boundaries, defects, interfacial chemical bonds, and mesoporous structures, endowing the SnO_2@TiO_2/C nanocomposite with a high reversible capacity of 830.7 mA h g^{-1} after 100 cycles at 0.5C, 438.5 mA h g^{-1} after 1000 cycles at 10C, and 217.7 mA h g^{-1} at 50C in the half cell. In the full cell, a high energy density of 328.4 and 245.9 W h kg^{-1} is achieved at 0.1 and 1C, respectively. These lithium ion storage performances are superior to those of previously reported TiO_2-based anodes.

Conflicts of interest

There are no conflicts of interest to declare.

Acknowledgements

The work was provided technical support by ''Ceshigo Research Service agency for TEM, www.ceshigo.com''.

References

1 S. Cao, Z. Xue, C. Yang, J. Qin, L. Zhang, P. Yu, S. Wang, Y. Zhao, X. Zhang and R. Liu, *Nano Energy*, 2018, **50**, 25–34.
2 S. Wang, Y. Yang, W. Quan, Y. Hong, Z. Zhang, Z. Tang and J. Li, *Nano Energy*, 2017, **32**, 294–301.
3 K. J. Hong and S. O. Kim, *Energy Storage Mater.*, 2016, **2**, 27–34.
4 M. Zhang, K. Yin, Z. D. Hood, Z. Bi, C. A. Bridges, S. Dai, Y. S. Meng, M. P. Paranthaman and M. Chi, *J. Mater. Chem. A*, 2017, **5**, 20651–20657.
5 F. Shahvaranfard, M. Altomare, Y. Hou, S. Hejazi, W. Meng, B. Osuagwu, N. Li, C. J. Brabec and P. Schmuki, *Adv. Funct. Mater.*, 2020, 1909738.
6 C. Gao, T. Wei, Y. Zhang, X. Song, Y. Huan, H. Liu, M. Zhao, J. Yu and X. Chen, *Adv. Mater.*, 2019, **31**, 1806596.
7 S. Liu, Z. Wang, C. Yu, H. B. Wu, G. Wang, Q. Dong, J. Qiu, A. Eychmüller and X. W. (David) Lou, *Adv. Mater.*, 2013, **25**, 3462–3467.
8 Y. Ren, Z. Liu, F. Pourpoint, A. R. Armstrong, C. P. Grey and P. G. Bruce, *Angew. Chem., Int. Ed.*, 2012, **51**, 2164–2167.
9 S. Tian, A. Xing, H. Tang, Z. H. Bao and G. M. Wu, *J. Mater. Chem. A*, 2014, **2**, 2896–2900.
10 R. Mo, Z. Lei, K. Sun and D. Rooney, *Adv. Mater.*, 2014, **26**, 2084–2088.
11 Q. Wu, J. Xu, X. Yang, F. Lu, S. He, J. Yang, H. Fan and M. Wu, *Adv. Energy Mater.*, 2015, **5**, 1401756.
12 S. Huang, L. Zhang, X. Lu, L. Liu, L. Liu, X. Sun, Y. Yin, S. Oswald, Z. Zou, F. Ding and O. G. Schmidt, *ACS Nano*, 2017, **11**, 821–830.
13 Y. Xing, S. Wang, B. Fang, G. Song, D. P. Wilkinson and S. Zhang, *J. Power Sources*, 2018, **385**, 10–17.
14 C. Chen, Y. Yang, S. Ding, Z. Wei, X. Tang, P. Li, T. Wang, G. Cao and M. Zhang, *Energy Storage Mater.*, 2018, **13**, 215–222.
15 M. Han, Z. Lin and J. Yu, *J. Mater. Chem. A*, 2019, **7**, 4804–4812.
16 Q. Wu, J. Xu, X. Yang, F. Lu, S. He, J. Yang, H. Fan and M. Wu, *Adv. Energy Mater.*, 2014, **5**, 1401756.
17 A. Magasinski, P. Dixon, B. Hertzberg, A. Kvit, J. Ayala and G. Yushin, *Nat. Mater.*, 2010, **9**, 353–358.
18 J. Qiu, C. Lai, Y. Wang, S. Li and S. Zhang, *Chem. Eng. J.*, 2014, **256**, 247–254.
19 A. Mondal, S. Maiti, K. Singha, S. Mahanty and A. B. Panda, *J. Mater. Chem. A*, 2017, **5**, 23853–23862.
20 M. Han and J. Yu, *Diamond Relat. Mater.*, 2018, **87**, 10–17.
21 M. Han and J. Yu, *Energy Technol.*, 2019, **7**, 1900084.
22 X. Tian, X. Li, T. Yang, K. Wang, H. Wang, Y. Song, Z. Liu, Q. Guo and C. Chen, *Electrochim. Acta*, 2017, **247**, 1060–1071.
23 Y. Zhou, R. Ma, S. L. Candelaria, J. Wang, Q. Liu, E. Uchaker, P. Li, Y. Chen and G. Cao, *J. Power Sources*, 2016, **314**, 39–48.
24 Q. Guo, Z. Zheng, H. Gao, J. Ma and X. Qin, *J. Power Sources*, 2013, **240**, 149–154.
25 S. Kang, X. Chen and J. Niu, *Nano Lett.*, 2018, **18**, 467–474.
26 H.-K. Roh, M.-S. Kim, K. Y. Chung, M. Ulaganathan, V. Aravindan, S. Madhavi, K. C. Roh and K.-B. Kim, *J. Mater. Chem. A*, 2017, **5**, 17506–17516.
27 S. Sakthivel and H. Kisch, *Angew. Chem., Int. Ed.*, 2003, **42**, 4908–4911.
28 R. Tian, Y. Zhang, Z. Chen, H. Duan, B. Xu, Y. Guo, H. Kang, H. Li and H. Liu, *Sci. Rep.*, 2016, **6**, 19195.
29 D. Li, S. Dai, J. Li, C. Zhang, M. Richard-Plouet, A. Goullet and A. Granier, *J. Electron. Mater.*, 2018, **47**, 7372–7379.
30 L. Sun, H. Si, Y. Zhang, Y. Shi, K. Wang, J. Liu and Y. Zhang, *J. Power Sources*, 2019, **415**, 126–135.
31 S. Kang, X. Chen and J. Niu, *Nano Lett.*, 2017, **18**, 467–474.
32 X. Zhuang, P. Song, G. Chen, L. Shi, Y. Wu, X. Tao, H. Liu and D. Zhang, *ACS Appl. Mater. Interfaces*, 2017, **9**, 28464–28472.
33 Y. S. Jung, P. Lu, A. S. Cavanagh, C. Ban, G.-H. Kim, S. H. Lee, S. M. George, S. J. Harris and A. C. Dillon, *Adv. Energy Mater.*, 2013, **3**, 213–219.
34 N.-S. Choi, Y. Lee, S.-S. Kim, S.-C. Shin and Y.-M. Kang, *J. Power Sources*, 2010, **195**, 2368–2371.
35 J. Chong, S. Xun, H. Zheng, X. Song, G. Liu, P. Ridgway, J. Wang and V. S. Battaglia, *J. Power Sources*, 2011, **196**, 7707–7714.

36 H. J. Kwon, J.-Y. Hwang, H.-J. Shin, M.-G. Jeong, K. Y. Chung, Y.-K. Sun and H.-G. Jung, *Nano Lett.*, 2020, **20**, 625–635.

37 H. J. Kim, S. Choi, S. J. Lee, M. W. Seo, J. G. Lee, E. Deniz, J. L. Yong, E. K. Kim and W. Choi, *Nano Lett.*, 2016, **16**, 282–288.

38 S. Chen, L. Shen, P. A. van Aken, J. Maier and Y. Yu, *Adv. Mater.*, 2017, **29**, 1605650.

39 W. He, Y. Liang, H. Tian, S. Zhang, Z. Meng and W. Q. Han, *Energy Storage Mater.*, 2017, **8**, 119–126.

40 H. Xiong, H. Yildirim, E. V. Shevchenko, V. B. Prakapenka, B. Koo, M. D. Slater, M. Balasubramanian, S. K. R. S. Sankaranarayanan, J. P. Greeley, S. Tepavcevic, N. M. Dimitrijevic, P. Podsiadlo and C. S. Johnson, *J. Phys. Chem. C*, 2012, **116**, 3181–3187.

41 N. Plylahan, M. Letiche, M. K. S. Barr, B. Ellis, S. Maria, T. N. T. Phan, E. Bloch, P. Knauth and T. Djenizian, *J. Power Sources*, 2015, **273**, 1182–1188.

42 M. Han, Y. Mu, F. Yuan, J. Liang, T. Jiang, X. Bai and J. Yu, *J. Mater. Chem. A*, 2020, **8**, 3822–3833.

43 M. Han and J. Yu, *J. Power Sources*, 2019, **414**, 435–443.